Lab on a Chip

PAPER

View Article Online
View Journal

Cite this: DOI: 10.1039/d5lc00775e

Carbonate reservoir surface-mimicking platform for CO_2–seawater–concrete flooding

Abhishek Ratanpara, Daniel Guerrero, Diana Cho, Abhishek, Adib Mahmoodi Nasrabadi and Myeongsub Kim *

Microfluidic platforms are increasingly used in enhanced oil recovery (EOR) studies due to their ability to visualize and control fluid displacement at the pore scale. While many designs successfully replicate reservoir geometries, mimicking realistic surface chemistry remains a challenge. To address this demand, we developed a microfluidic platform using polydimethylsiloxane (PDMS) mixed with calcium carbonate ($CaCO_3$) powder to emulate both the structure and oil-wet surface characteristics of carbonate rocks. Sessile droplet tests confirmed strong oil-wet behavior, with contact angles of 138.55° in deionized (DI) water and 130.9° in seawater on an oil-coated $CaCO_3$-based PDMS surface. Additionally, fluorescence microscopy verified oil retention within the composite surface, indicating its absorption capacity. Moreover, homogeneous and randomly structured porous networks were fabricated to assess flooding performance. A concrete-based carbonated seawater solution, enriched with calcium ions (Ca^{2+}) and carbonate species like bicarbonate and carbonate ions, was used as a flooding fluid for EOR. In the homogeneous network, this solution achieved approximately 20% of the original oil in place (OOIP) recovery, compared to 25% OOIP with SDS. In the random network, where pore-scale heterogeneity presents greater flow resistance, oil recoveries were found to be 30.4% of OOIP and 39.98% of OOIP, respectively. These results highlight the synergistic effect of engineered surface chemistry and chemically active fluids in promoting oil displacement under varied flow conditions.

Received 7th August 2025,
Accepted 14th November 2025

DOI: 10.1039/d5lc00775e

rsc.li/loc

1. Introduction

Global energy demand increased by 2.2% in 2024, nearly twice the average growth rate of the past decade, driven by rapid technological development and expanding industrial activity worldwide.[1] Although renewable energy sources continue to grow, they remain insufficient to fully meet this accelerating demand. Consequently, fossil fuels still account for nearly 80% of global energy supply, with oil demand alone rising by 0.8% in 2024.[1] Conventional extraction methods typically recover only 30–35% of the original oil in place, which led to the introduction of EOR techniques aimed at extracting the remaining trapped oil.[2] While EOR has helped improve recovery rates, the depletion of shallow reservoirs is prompting exploration to shift toward deeper, more geologically complex formations. These new targets often feature tighter pore networks and more variable mineral compositions, making recovery even more challenging.[3,4] This evolving landscape highlights the need for more focused and accelerated research in EOR methods.

Given the growing challenges in oil recovery from complex reservoirs, there has been an increasing reliance on laboratory-scale tools that enable precise visualization of fluid transport and interfacial behavior at the pore scale, thereby accelerating research progress.[5] While conventional core flooding has long served as a foundational technique in EOR research, it is often limited by its lack of optical accessibility, slower experimental cycles, and reduced flexibility in testing a wide range of fluid formulations and recovery methods.[6] To overcome these limitations, microfluidic platforms, commonly known as a reservoir on a chip system, have gained widespread adoption over the past two decades. These systems offer direct insight into displacement patterns, wettability alterations, and flow regimes within porous networks.[7] Early contributions by Tsakiroglou and Avraam utilized LIGA-fabricated poly(methyl methacrylate) (PMMA) micromodels with pore depths ranging from 10 to 100 μm with controllable aspect ratios, enabling high-resolution imaging of meniscus dynamics and fluid displacement.[8] Expanding on this, Yun *et al.* fabricated dual-depth silicon micromodels that mimic carbonate heterogeneity, incorporating micropores and macropores with pore widths ranging from 1.5 to 21 μm and depths ranging from 7 to 14 μm to study capillary trapping and flow

Department of Ocean and Mechanical Engineering, Florida Atlantic University, Boca Raton, FL 33431, USA. E-mail: kimm@fau.edu

dynamics.[9] Alomier *et al.* further advanced the field by developing micromodels with spatially controlled wettability using soft lithography and vapor-phase salinization, achieving sub-millimeter pore geometries while introducing independently tunable wetting domains as small as 50 μm in width.[10] This enabled, for the first time, direct observation of fluid displacement and saturation dynamics across sharply contrasting wetting regions within a single micromodel, offering insights into mixed-wettability effects that were previously unresolvable in uniformly treated or chemically homogeneous chips. More recently, Godoy *et al.* introduced a rock-on-a-chip approach that converts CT-scanned porous media into quasi two-dimensional microfluidic devices, replicating pore and throat size distributions with over 90% precision and a channel depth of 21 μm, while achieving permeability values consistent with those of the original rock samples.[11] These innovations have significantly reduced the experimental turnaround time from several days or weeks in traditional core flooding setups to just a few hours, demonstrating how microfluidic channels have advanced the study of geometric complexity and pore-scale mechanisms in enhanced oil recovery research.

Although recent advancements have enabled high-fidelity replication of pore geometry, reproducing reservoir-representative surface properties within microfluidic devices remains a persistent challenge.[12] One widely used method involves the *in situ* growth of calcium carbonate by injecting supersaturated solutions of calcium and carbonate ions.[13] While this approach can introduce carbonate mineral features, it often results in uneven deposition, localized throat clogging, and poor long-term adhesion under fluid flow. Alternatively, nanocrystalline calcium carbonate coatings applied *via* dip-coating, or layer-by-layer assembly have shown initial success in mimicking surface chemistry.[14] However, these coatings frequently suffer from delamination, inconsistent thickness, and mechanical instability during prolonged exposure to brines or surfactants. In contrast, direct acid-etching of natural calcite substrates has been shown to retain the native mineralogy and microtexture.[15] Yet this method sacrifices geometric precision and optical clarity, limiting its suitability for controlled visualization studies. Collectively, these limitations emphasize the need for more robust surface engineering strategies that preserve both chemical authenticity and experimental reliability within microfluidic platforms.

To address the gap in replicating surface chemistry, this study presents a novel approach using a composite microfluidic platform composed of polydimethylsiloxane and calcium carbonate (PDMS–$CaCO_3$). PDMS is widely used due to its optical transparency, ease of fabrication, and mechanical resilience, and is naturally hydrophobic and oleophilic.[16] It readily absorbs oil because its polymer matrix contains methyl groups that interact favorably with hydrocarbons, allowing for diffusion into the bulk material through van der Waals forces.[17] However, despite these properties, PDMS does not replicate the surface chemistry of carbonate reservoirs, which plays a crucial role in controlling wettability and interfacial behavior. By integrating $CaCO_3$ into the PDMS matrix, this work introduces carbonate-specific interfacial characteristics while retaining the structural and optical advantages of PDMS, better suited for pore-scale displacement studies. As a demonstration of utility, the platform was also used to evaluate the performance of carbonated seawater-based concrete (seawater–concrete–CO_2) solution, representing a possible post-carbon-capture flooding formulation.

This fluid comes from the unique chemical profile of the carbonated seawater–concrete solution, which contains both dissolved CO_2 and alkaline mineral residues. The dissolved CO_2 lowers the brine pH, and a low pH is known to drive carbonate systems toward a strongly water-wet state due to H^+ adsorption at the oil-brine and brine-carbonate interfaces, which facilitates oil detachment.[18] With seawater–concrete solution with dissolved CO_2, the CO_2-driven wettability shift is combined with additional ionic effects from waste concrete and seawater mixture, which is enriched with calcium and magnesium ions leached from the concrete, alongside native seawater salinity components such as Na^+, Cl^-, and SO_4^{2-}. Prior studies have demonstrated that divalent cations such as Ca^{2+} and Mg^{2+} can significantly enhance oil recovery by altering surface charge, promoting favorable wettability shifts, and suppressing fines migration in carbonate formations.[19] Together, these effects suggest that the seawater–concrete–CO_2 solution may offer synergistic benefits for EOR, combining chemical triggers known from smart waterflooding with the added functionality of integrated carbon utilization. Evaluating this fluid within a carbonate-mimicking microfluidic environment provides a mechanistic perspective on its displacement performance and offers insight into its viability as a post-capture flooding agent. This work highlights a fabrication strategy that enhances the ability of microfluidic systems to mimic carbonate reservoir surfaces, thereby expanding their application for studying multiphase flow under more geochemically relevant conditions.

2. Materials and methods

2.1. Materials

The microfluidic channel was fabricated using a mixture of PDMS and $CaCO_3$. The PDMS elastomer kit (Sylgard™ 184 Silicone Elastomer Kit) was purchased from Dow Corning (Midland, MI, USA), and $CaCO_3$ powder was obtained from Fisher Scientific (Fisher Chemical C114-500, Fair Lawn, NJ, USA). The oil used in the flooding experiments was Light Texas Crude Oil, with a density of 796 kg m^{-3} and viscosity of 27.26 cP. For preparing different flooding fluids, sodium dodecyl sulfate (SDS, >99% purity) was purchased from Sigma-Aldrich (St. Louis, MO, USA). Natural seawater was collected from the Atlantic Ocean along the coast of Boca Raton, Florida. The salinity of the seawater, measured using

a salinity tester (HI98319, Hanna Instruments), was found to be 34.3 g kg^{-1}. The concrete mix was purchased from Quikrete Holdings, Inc. CO_2 gas (Research 5.0 Grade, 99.999% purity) was supplied by Airgas, Inc. (Radnor, PA, USA). pH measurements were recorded using a Hanna Edge portable pH probe with an accuracy of ±0.01 pH units. The flow setup utilized Teflon® PTFE semi-clear tubing (1/32″ ID, 1/16″ OD) purchased from McMaster-Carr (Elmhurst, IL, USA) and a syringe pump (Harvard Apparatus 11 Pico Plus Elite, Holliston, MA, USA). X-ray micro-CT imaging was performed using a Bruker SkyScan 1273 system, and surface topography measurements were obtained using a Keyence optical 3-D profilometer (VR-6000 Series).

2.2. Microfluidic channel design and fabrication

To investigate the role of pore geometry in multiphase transport, we designed two microfluidic networks: one with a geometrically homogeneous structure and another with a random structure (Fig. 1a and b). Both networks share identical outer dimensions (20 mm × 0.5 mm × 40 mm) and were interfaced with symmetric bifurcating inlet and outlet channels to ensure uniform flow distribution. The inlet begins as a 2 mm-diameter circular port, which transitions into a straight, 8 mm-long, 2 mm-wide channel. This primary channel then bifurcates into two parallel branches (each 2 mm wide and 8 mm long), which further split into four 1 mm-wide, 8 mm-long channels that feed into the porous domain (Fig. 1c). This configuration minimizes entrance effects and promotes balanced flow across the network width. In both types of networks, the depth was kept at 500 μm. To facilitate mold release, a 5° vertical taper was applied to the sidewalls in both geometries. The homogeneous network consists of a 13 × 26 array of square pillars, each with a 1 mm × 1 mm footprint, and uniformly spaced by 500 μm gaps, forming well-defined flow paths throughout the domain. The total pore volume was approximately 231 μL with a porosity of 0.58. The random network was generated by first creating a 2D grid of random values and then applying a Gaussian blur technique to introduce smooth spatial variation. To achieve the desired porosity, the structure was converted into a binary map by selecting a threshold value, where higher values were considered as pores and lower values as the solid region. In this study, we arbitrarily selected a porosity of 50% and a pore volume of approximately 100 μL. The resulting pattern includes irregular pore shapes and connectivity, making it suitable for simulating disordered flow conditions. Using the Kozeny–Carman relation with literature-reported ranges for the geometry constant $C \approx 5$–200 and tortuosity $\tau \approx 1$–1.3 for the homogeneous network and $\tau \approx 1.5$–3 for the random network, the estimated permeabilities fall within approximately 10^3–10^4 Darcy for the homogenous network and 10^2–10^3 Darcy for the random network.[20–24] These values are provided solely as theoretical reference ranges, as they do not affect the experimental comparisons performed within the same device geometry.

The channel designs were created in SolidWorks software. Master molds were fabricated using a FormLab 3B+ SLA 3D

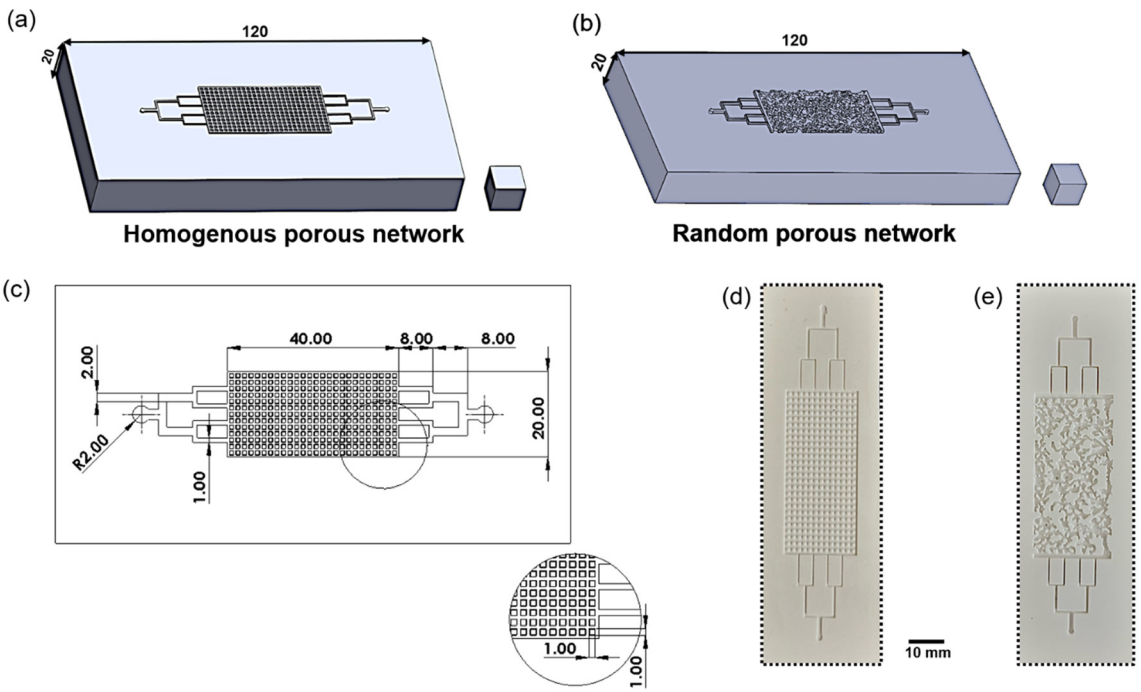

Fig. 1 (a and b) 3D models illustrating the patterns of homogeneous and random porous networks. The right panel shows the geometric layout with all corresponding measurements. The cube in both 3D models represents a 1 mm × 1 mm × 1 mm scale. The channel print is 0.5 mm embossed from the surface. (c) Geometrical layout of channels. Actual image of the fabricated microchannel networks for (d) homogeneous and (e) heterogeneous geometries. All dimensions are in mm scale.

printer with Model V2 resin, as shown in Fig. 2a. After printing, molds were cleaned with isopropyl alcohol (IPA) for 30 minutes and cured under UV light for an additional 30 minutes. A mixture of PDMS, $CaCO_3$, and curing agent in the ratio 67 : 100 : 14 was thoroughly mixed and cast onto the master mold (Fig. 2b). This ratio was determined through iterative trial and error to ensure a uniform distribution of $CaCO_3$ particles across the channel surfaces while maintaining a sufficient amount of curing agent to achieve complete crosslinking and structural integrity of the composite. Due to the high viscosity of the composite, the casting process was performed in two stages to prevent air entrapment and ensure complete filling of the microfeatures. First, a thin layer was poured and degassed for 30 minutes, followed by a second layer that was degassed for 3 hours. After degassing, the mold was placed in an oven at 60 °C for 8 hours to cure the composite (Fig. 2c). Once cured, the patterned composite slab was carefully demolded and trimmed. A matching transparent PDMS layer was prepared separately using conventional soft lithography on a flat surface.[25] After curing and punching inlet/outlet holes, the composite and transparent layers were bonded using a thin coating of curing agent and post-cured at 60 °C for 15 minutes to complete the assembly (Fig. 2f). The PTFE tubes were then inserted in the inlet and outlet with epoxy to ensure a leakage-free connection. To verify that the PDMS–$CaCO_3$ surface did not introduce unintended roughness-driven effects and to confirm that $CaCO_3$ was uniformly present at the exposed channel interface, 3-D optical profilometry and X-ray micro-CT scanning were performed. The measurements showed moderate roughness and a spatially uniform distribution of $CaCO_3$ up to the channel surface without visible agglomeration (see SI).

2.3. Contact angle measurements *via* sessile droplet method

To verify the oil-wetting characteristics of the proposed PDMS–$CaCO_3$ channel and evaluate its carbonate surface–mimicking behavior, sessile droplet tests were conducted. As shown in Fig. 3, the setup consisted of a PMMA-based chamber with a submerged stage to hold solid specimens in each liquid. Tests were performed in both deionized (DI) water and seawater to simulate relevant microfluidic flooding environments. A syringe pump was used to dispense controlled volumes of oil droplets, which rose and adhered to the specimen surface upon contact (see Video S1). The system included a backlight imaging setup and a horizontally aligned calibrated camera to capture the droplet profile at the solid–liquid–oil interface. Recorded videos were analyzed using ImageJ to determine the static contact angles. This setup was used to compare the wettability of the PDMS–$CaCO_3$ composite surface with that of conventional PDMS.

2.4. Microfluidic flooding test

To evaluate the flooding performance of the proposed microfluidic chip, a series of multiphase displacement experiments was conducted using both homogeneous and random pore network geometries. In addition, the novel seawater–concrete solution enriched with dissolved CO_2 (10 g L^{-1} concrete) was tested and compared against commonly used surfactant flooding fluids, along with control DI water and natural seawater. The concrete concentration in natural

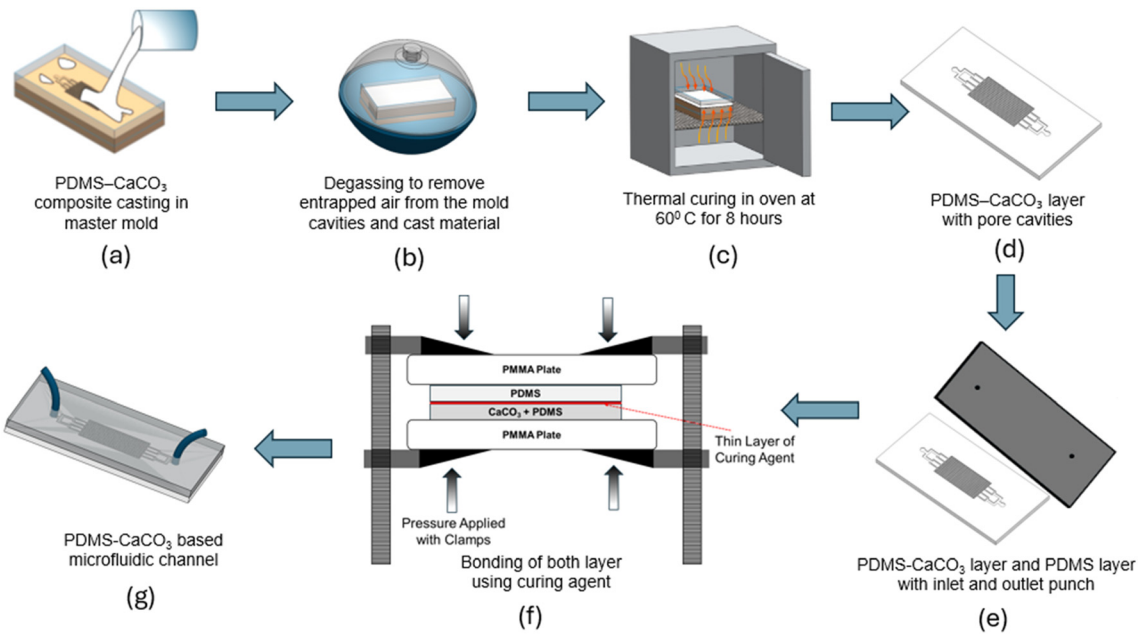

Fig. 2 Fabrication procedure for the PDMS–$CaCO_3$ microfluidic device: (a) mold casting, (b) degassing, (c) curing, (d) trimming the bottom channel with pore cavity, (e) preparing the top PDMS layer, (f) bonding the PDMS–$CaCO_3$ and PDMS layers, and (g) connecting inlet and outlet tubing.

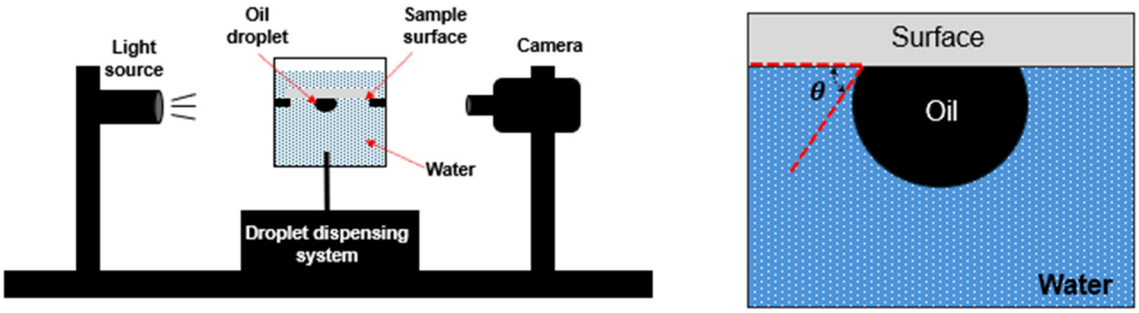

Fig. 3 Experimental setup for a sessile droplet test to measure an oil–liquid–solid contact angle to evaluate surface wettability.

seawater is selected based on the optimization of alkaline ion concentration in our previous study.[26] DI water-based SDS solution (10 g L^{-1}) solution (10 g L^{-1}) was prepared by stirring with a magnetic stirrer for 15 minutes at 1000 rpm. For the seawater–concrete solution, concrete powder was added to seawater and stirred magnetically, followed by continuous CO_2 bubbling until the pH decreased from approximately 10 to 5, indicating effective CO_2 dissolution. As shown in Fig. 4, the experimental setup featured a rigid PMMA holder designed to secure the chip and prevent deformation during the injection process. Prior to each test, the microfluidic chips were aged in crude oil at ambient conditions for 12 hours to promote oil-surface interaction and establish a stable wetting state. Oil soaking was conducted by connecting a crude oil reservoir to both the inlet and outlet of the chip, allowing continuous exposure across the entire channel. Based on preliminary trial-and-error observations, the reduction in oil level in the connected reservoir ceased after approximately 12 hours, indicating saturation of the adsorption process. Given the consistent channel thickness and volume across chips, this duration reliably resulted in uniform oil saturation and representative wettability conditions. Flooding was performed at a constant flow rate of 15 μL min^{-1} using a syringe pump. Displaced oil was directed through PTFE tubing into a collection vial. Each experiment was run for 150 minutes, corresponding to approximately 8 times the total pore volumes, after which oil recovery was found to be insignificant. The displacement process was recorded using a top-mounted camera, and image sequences were analyzed using custom MATLAB scripts. All experiments were repeated in triplicate to ensure reproducibility.

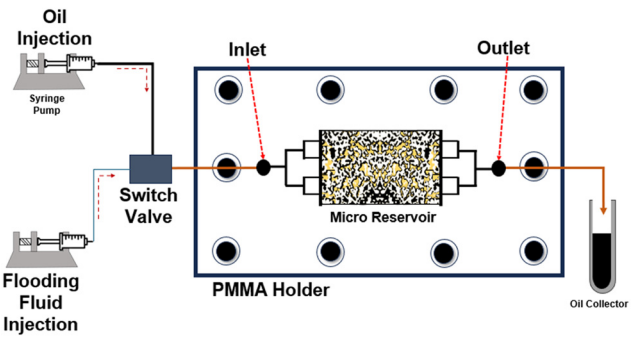

Fig. 4 Schematic of the flooding experiment setup, including two syringe pumping systems, a switch valve, and a microfluidic platform.

3. Results and discussion

3.1. Sessile droplet test

To characterize the wettability of the fabricated surfaces, time-resolved sessile droplet tests were performed using both PDMS and PDMS–$CaCO_3$ substrates submerged in DI water and seawater. For each case, crude oil droplets were introduced, and videos were recorded to track the evolution of the contact angle over time. The videos were analyzed using ImageJ to extract contact angle data.

As shown in Fig. 5, all surfaces exhibited a rapid increase in contact angle that stabilized within 120 seconds, indicating a quasi-equilibrium wetting state. At equilibrium, the PDMS–$CaCO_3$ surface exhibited stronger oil-wet behavior compared to unmodified PDMS. Specifically, the final contact angles on the PDMS–$CaCO_3$ surface reached 138.55° in DI water and 130.9° in seawater, whereas the PDMS surface showed contact angles of 121.85° and 120.35°, respectively. All measured angles were above 120°, confirming the strong

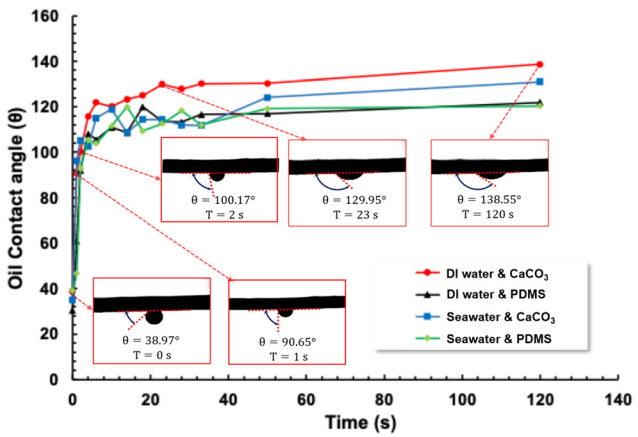

Fig. 5 Time-dependent oil contact angle measurements on PDMS–$CaCO_3$ and PDMS surfaces in DI water and seawater. The five experimental images show oil droplet profiles at different times (0 s, 1 s, 2 s, 23 s, and 120 s) on the PDMS–$CaCO_3$ surface immersed in DI water.

oil-wet characteristics of both materials.[27] The slightly reduced contact angles in seawater compared to DI water are consistent with findings from previous studies, which suggest that multivalent cations such as Ca^{2+} and Mg^{2+} in seawater can adsorb at solid and oil interfaces and interfere with polar interactions between crude oil and the surface.[18,28] These ions may form hydration layers or alter the surface affinity for polar oil components, leading to a modest reduction in oil adhesion. Nevertheless, the PDMS–$CaCO_3$ composite retained a higher contact angle than PDMS in both aqueous environments, supporting its effectiveness in mimicking carbonate surfaces for microfluidic oil recovery studies.

3.2. Fluorescence imaging for oil absorption

To further validate the oil-wet characteristics of the PDMS–$CaCO_3$ composite surface and its functional similarity to carbonate reservoir rocks, an oil absorption test was conducted *via* fluorescence imaging. While sessile droplet measurements confirmed strong oil-wet behavior, this complementary test was designed to directly visualize oil retention within the channel walls after prolonged exposure. The microchannel was filled with crude oil and aged under ambient conditions for 12 hours to allow sufficient time for potential oil absorption into the composite structure. Following aging, all injected oil was carefully drained from the channel using suction, ensuring that only the oil absorbed or strongly retained by the surface remained. The channel was then cross-sectioned and imaged under fluorescence microscopy using a UV light source to excite the crude oil. As shown in Fig. 6, a strong fluorescent signal was observed at the PDMS–$CaCO_3$ surface, arising from the autofluorescence of crude oil retained in the composite.[29] In contrast, no fluorescence was detected in a reference PDMS–$CaCO_3$ channel that had not been exposed to oil, confirming that the observed signal originates from retained oil rather than background material properties.

These results provide further evidence of the surface's strong affinity for crude oil. Although the overall $CaCO_3$ content in the PDMS–$CaCO_3$ composite channel is relatively lower (37%) than that of PDMS, the surface-exposed $CaCO_3$ fraction is sufficient to impart mineral characteristics that enhance oil retention on the channel surface. This observation aligns with previous reports, which show that even partial exposure of carbonate minerals can lead to a strong interaction with polar components in crude oil. Moreover, in natural carbonate reservoir rocks, silicates and clays are often present and are known to reduce oil-wetness. Since these are absent in the fabricated surface, it could arguably be more oil-wet than the actual reservoir rock surface.

3.3. Flooding performance in homogeneous microfluidic network

Previous sections established the oil-wet nature of the proposed novel PDMS–$CaCO_3$ microfluidic chip based on sessile droplet measurements and fluorescence-based tests.

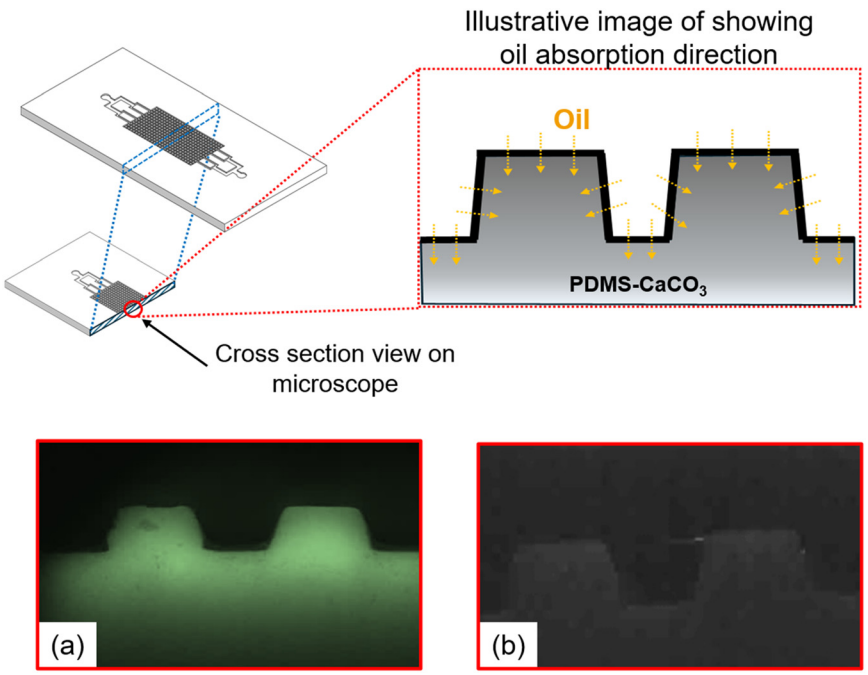

Fig. 6 Schematic of the PDMS–$CaCO_3$ microchannel and fluorescence microscopy validation of oil absorption. The magnified cross-section highlights oil uptake (yellow arrows) into the micropillar walls and base. (a) Oil-exposed channel shows strong fluorescence, confirming oil absorption. (b) The control channel shows no fluorescence, indicating no oil presence; image brightness was enhanced for visibility due to low signal in the dark field.

In oil-wet porous systems, fluid displacement behavior is primarily governed by two dimensionless parameters: the Capillary number (Ca) and the mobility ratio (M).[30] Ca quantifies the ratio of viscous to capillary forces and is defined as:

$$\mathrm{Ca} = \frac{\mu_d U}{\gamma} \quad (1)$$

where μ_d is the viscosity of the displacing phase, U is the average velocity of the displacing phase, and γ is the interfacial tension (IFT) between oil and the displacing fluid. The mobility ratio is commonly defined as:

$$M = \frac{k_{rw}/\mu_w}{k_{ro}/\mu_0} \quad (2)$$

where, k_{rw} and k_{ro} are relative permeabilities of the displacing fluid (*e.g.*, water) and displaced fluid (*e.g.*, oil), respectively, representing their effective flow capacity in the presence of each other. However, in microfluidic experiments, absolute or relative permeabilities are not directly measurable or even well-defined due to the idealized geometry.[31] Therefore, a modified form of M is widely adopted, simplified as the ratio of fluid viscosities:

$$M = \frac{\mu_0}{\mu_w} \quad (3)$$

This simplification allows for the estimation of flow stability and viscous dominance using only fluid properties. In our experiments, Texas light crude oil, with a viscosity of approximately 60 mPa s and a density of approximately 0.85 g cm^{-3}, was used as the displaced phase. The viscosity of all aqueous flooding fluids was close to 1 mPa s. Based on reported literature values, the IFT was conservatively assumed to be 30 mN m^{-1} as an upper bound for non-surfactant fluids, to ensure consistent and cautious estimation of the capillary number.[32–36] The flow rate was fixed at 15 μL min^{-1}, and the channel cross-sectional area was 6.75 mm^2, yielding an average velocity of ~0.037 cm s^{-1}. Substituting these values into the equations for M and Ca yields 60 and 1.23 × 10^{-5}. Based on the Lenormand phase diagram, these values indicate a capillary-dominated regime.[37] In such a regime, displacement is typically inefficient due to capillary trapping, and improvements are primarily achieved through reductions in interfacial tension or alterations in wettability. To evaluate the influence of these parameters, we tested four different flooding fluids in the homogeneous porous microfluidic chip: DI water, seawater, a seawater–concrete solution with dissolved CO_2, and SDS solution. Oil recovery was quantified as a percentage of the original oil in place using image analysis of flooding sequences. Fig. 7 shows the oil recovery during the flooding test in each test solution over time. It shows the oil recovery was measured with respect to the amount of initial oil in the reservoir.

DI water yielded the lowest oil recovery, approximately 10% for 150 minute flooding. As it lacks ions or surface-active agents, it neither alters surface wettability nor significantly changes the IFT. This leads to poor displacement efficiency under low-Ca conditions, where capillary forces dominate. Seawater provided moderately improved oil recovery of approximately 15%, primarily due to its ionic composition, particularly multivalent cations like Ca^{2+} and Mg^{2+}, which can promote surface wettability alteration toward more water-wet conditions. As observed earlier during the contact angle tests, the equilibrium contact angle was slightly reduced in seawater compared to DI water, supporting this effect. However, since the interfacial tension remained largely unchanged, the improvement in recovery was limited, resulting in only about a 5% higher recovery than that of deionized water. The SDS solution resulted in the highest oil recovery, around 25%. This is attributed to two primary mechanisms. First, SDS molecules adsorb at both the oil–water interface and the reservoir rock surface. At the oil–water interface, SDS lowers the interfacial tension by aligning its amphiphilic molecules at the boundary: the hydrophobic tails are attracted to the oil phase, while the hydrophilic sulfate heads remain in the aqueous phase. This disrupts the cohesive forces at the interface, making it more deformable and allowing trapped oil to mobilize more easily.[12] Second, at the reservoir rock surface, the negatively charged sulfate headgroups electrostatically interact with positively charged or polar groups on the surface. Once adsorbed, the hydrophilic heads remain exposed, increasing the surface's affinity for water and shifting the wettability toward a more water-wet condition. Together, these interfacial tension reduction and wettability alteration mechanisms explain the comparatively high performance of SDS in enhancing oil recovery.[12] These effects increase the Capillary number and suppress capillary trapping, promoting a more stable displacement front. The strong performance of SDS is consistent with extensive literature on chemical-enhanced oil recovery using surfactants.

The seawater–concrete–CO_2 solution achieved an intermediate recovery rate (~20%), higher than that of both

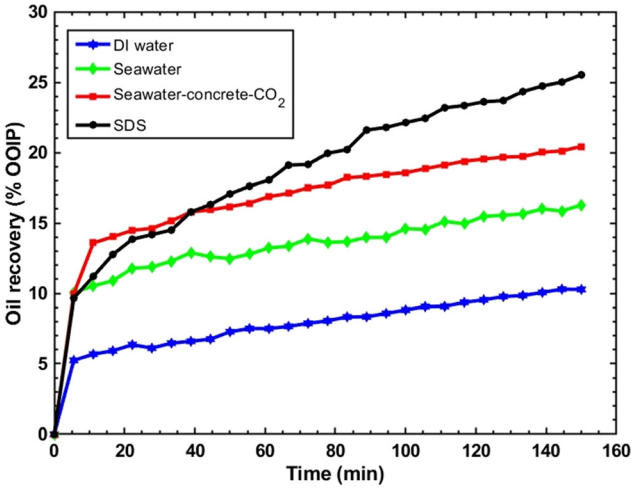

Fig. 7 Oil recovery in a homogeneous pore network during flooding with different fluids.

DI water and seawater, but lower than that of SDS. This improvement is likely due to the additional Ca^{2+} ions leached from the concrete and the formation of carbonate and bicarbonate species from dissolved CO_2. Divalent cations, such as Ca^{2+} and Mg^{2+}, can displace carboxylate groups that are electrostatically adsorbed onto the positively charged sites of carbonate reservoir surfaces, thereby freeing the surface and enhancing hydration. This promotes a transition toward more water-wet conditions. Bicarbonate ions can also adsorb onto the surface, modulating the local charge distribution and further supporting alterations in wettability.[19] While the IFT was assumed to remain near 30 mN m^{-1}, the improved recovery suggests that surface interactions played a dominant role in enhancing the displacement process. These findings illustrate how displacement efficiency in homogeneous porous media under low-Ca conditions can be significantly enhanced by fluids that either reduce IFT or modify surface wettability, with SDS providing the strongest effect through both mechanisms, and the proposed seawater–concrete solution showing promising performance through a chemical route consistent with low-salinity and smart water flooding strategies.

Fig. 8 presents direct experimental observations from the flooding process. On the left, the microchannel is shown at three time points during the oil aging stage: immediately after crude oil injection (T_0), after partial displacement (T_1), and at a later stage (T_2), showing oil saturation prior to flooding. The right panel displays actual images from the flooding test at 0 min, 5 min, and 150 min. These snapshots capture the progression of the displacement front through the homogeneous porous network. Oil was initially introduced and aged for 12 hours to establish stable oil-surface interaction before initiating flooding. The visual sequence clearly demonstrates the evolution of the displacement front, highlighting differences in flow behavior and residual trapping. The combination of image-based analysis and direct visualization provides strong support for the comparative performance of each fluid under capillary-dominated conditions.

3.4. Flooding performance in random microfluidic network

Flooding experiments were also conducted in a randomly structured porous network to evaluate fluid performance under heterogeneous conditions that better resemble natural carbonate reservoirs. Similar to the homogeneous tests, flooding behavior was analyzed using image-based techniques to visualize the progression of displacement and quantify local oil saturation. Fig. 9 illustrates the oil displacement process in the random network along with its image processing. The left panel presents selected experimental snapshots at various flooding time points, while the right panel displays the corresponding MATLAB-processed images, where pixel intensity was mapped to capture changes in local oil saturation. This visualization highlights the spatial progression of fluid displacement through the heterogeneous structure and provides additional context for interpreting differences in interfacial behavior among the flooding fluids.

Quantitative oil recovery results were extracted from the image data to compare the performance of all four flooding fluids under heterogeneous flow conditions. As shown in Fig. 10, SDS and seawater–concrete–CO_2 solutions achieved the highest recoveries at 39.98% and 30.4%, respectively. Seawater and DI water yielded lower values of 22.36% and 11.90%, consistent with trends observed in the homogeneous pattern. Interestingly, the overall oil recovery values in the random network were higher than those obtained in the homogeneous setup, despite its smaller pore volume. This can be attributed to differences in fluid advancement

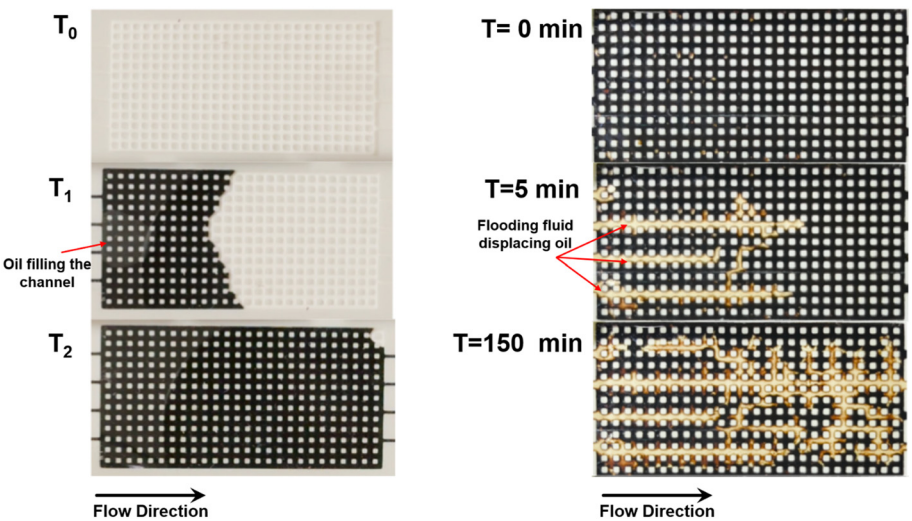

Fig. 8 Visual snapshots of oil distribution and fluid displacement in the homogeneous microfluidic chip at different times. The left column shows the progression of oil saturation (oil represented by the dark region); the right column captures the evolution of the displacement front during flooding (the flooding fluid is represented by the light region).

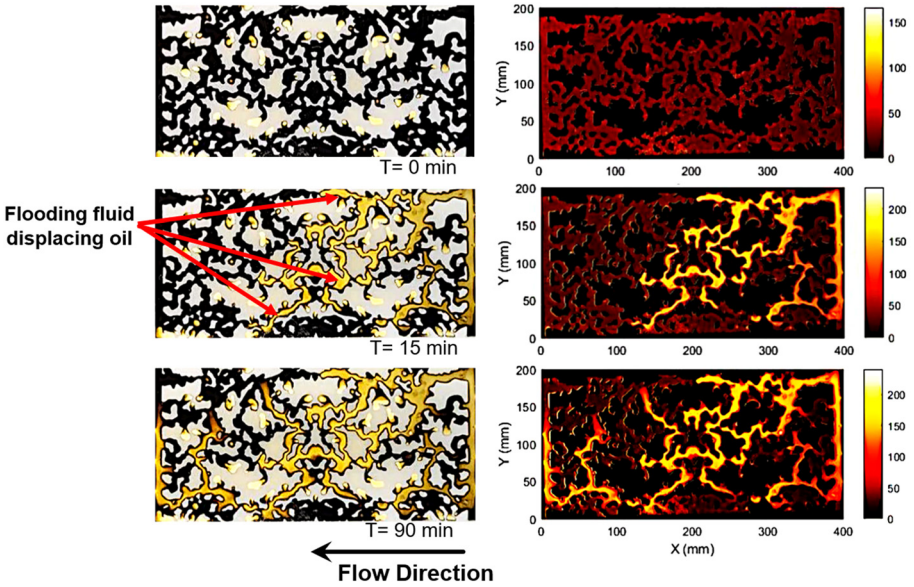

Fig. 9 Flooding progression in a randomly structured microfluidic network. Left: experimental snapshots at different time points (dark region represents oil and light region represents flooding fluid). Right: MATLAB-processed images showing pixel intensity mapping used to visualize oil displacement.

behavior, which are shaped by pore structure. In the homogeneous network, fluid tends to move in a straight path once a breakthrough occurs, creating a dominant flow channel and leaving large regions bypassed. In contrast, the random network contains irregular pore connectivity and non-linear flow paths, which may have promoted broader sweep and improved access to otherwise isolated pores. These structural characteristics could delay preferential channeling and encourage more uniform displacement. Datta *et al.* reported that disordered porous media enable more uniform front advancement and suppress fingering under capillary-driven conditions, enhancing fluid access to the entire pore network.[38] Similarly, Pak *et al.* demonstrated that disordered microstructures resulted in more extensive oil recovery and less trapping, attributed to enhanced capillary invasion dynamics.[39] Although further analysis is needed to confirm the exact mechanism in our case, the observed recovery trend in the random network may be linked to enhanced redistribution of flow paths and improved capillary access and plausibly by increased tortuosity, whereby longer and more irregular flow paths enhance capillary access and promote redistribution of trapped oil, a mechanism consistently observed in heterogeneous porous media in many studies.[40–42] These findings reinforce the importance of considering pore structure in evaluating the effectiveness of advanced flooding fluids.

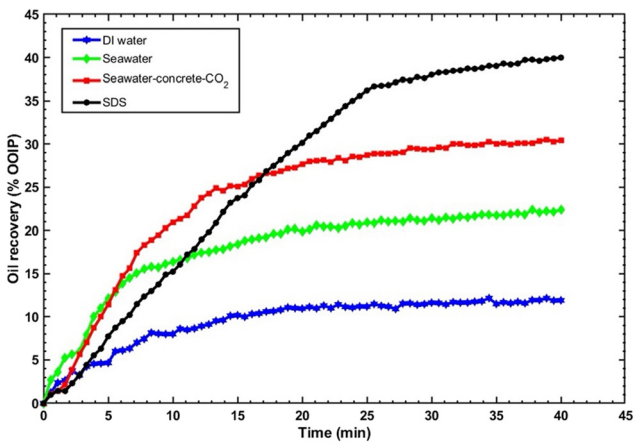

Fig. 10 Oil recovery in a random pore network during flooding with different fluids.

To better understand the mechanisms underlying this difference in recovery of both flooding fluids, the flooding videos were systematically analyzed to observe variations in interface behavior. Based on this analysis, several notable phenomena were identified, particularly in regions near narrow pore throats, where displacement performance differed significantly between the flooding fluids. Fig. 11 presents time-lapse snapshots captured at 8, 10, 15, and 30 minutes during flooding experiments, focused on the same region within the random porous network. Enlarged views of a representative pore throat show localized interfacial behavior. In the SDS flooding sequence, the interface clearly advances through the selected pore over time, indicating active displacement. In contrast, under seawater–concrete–CO_2 flooding, the oil remains largely pinned within the same pore throat, showing minimal movement across all time points. This behavior can be explained by the relatively weaker IFT reduction of the proposed solution, which may have limited its ability to overcome capillary entry pressures in tighter pore regions.

Moreover, the visual appearance of the flooded regions differed noticeably between the two cases. The SDS-flooded

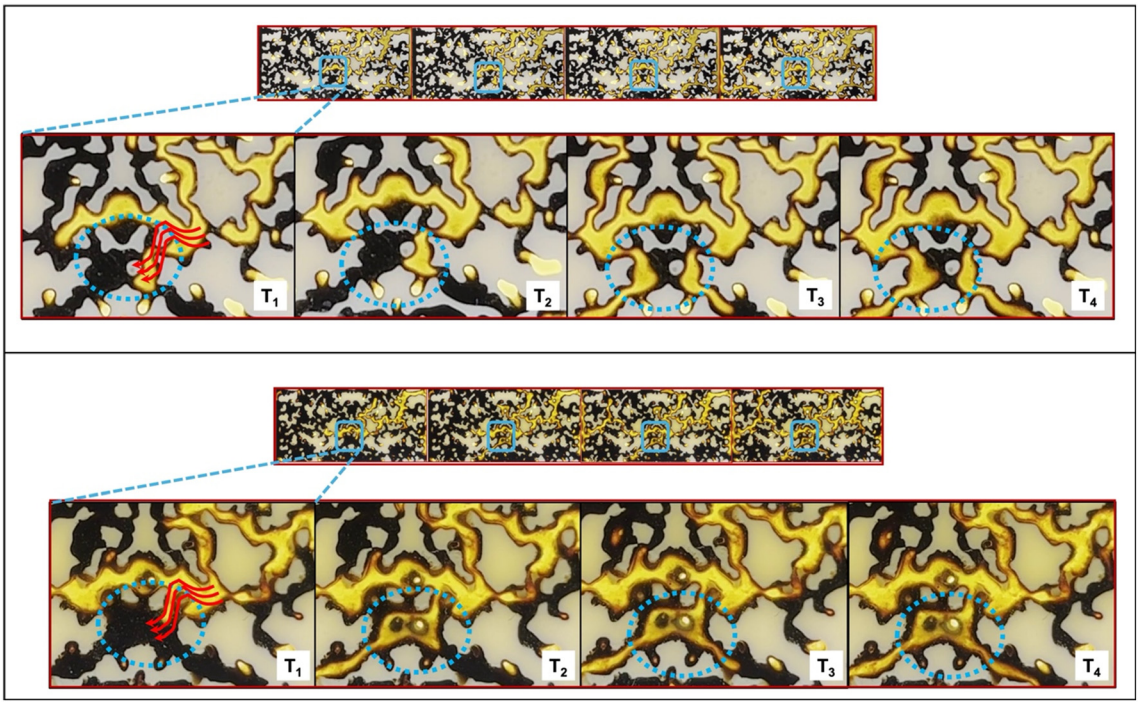

Fig. 11 Image sequence showing oil displacement in the random porous network using seawater–concrete–CO_2 (top) and SDS (bottom) flooding. Each sequence captures four time points: T_1 = 8 min, T_2 = 10 min, T_3 = 15 min, and T_4 = 30 min. The blue dotted circles indicate the region of interest used to observe pore-scale displacement.

areas appeared diffuse and slightly blurred, likely due to emulsified oil or residual surfactant layers. In contrast, channels flooded with the seawater–concrete–CO_2 solution appeared visually cleaner, with sharply defined boundaries and minimal oil residue. Although this clarity suggests more effective surface cleaning, the overall recovery indicates that surface interaction alone was not sufficient to surpass the displacement efficiency enabled by SDS. The cleaner appearance may result from adsorption-driven interactions, where Ca^{2+}, HCO_3^-, and high salinity promote electrostatic attraction to the channel surface, displacing surface-bound oil and modifying wettability. While the seawater–concrete–CO_2 solution did not match the recovery performance of SDS, it showed meaningful effectiveness under heterogeneous conditions. Its ability to interact with the carbonate-rich surface and leave visibly cleaner channels suggests favorable fluid–solid interactions that may support long-term displacement, particularly when flow conditions are favorable. These findings suggest that despite limited IFT reduction, the proposed solution presents a viable, surfactant-free alternative with sustainability advantages. With further optimization, its performance could approach that of conventional chemical agents, especially in complex reservoir-like environments.

4. Conclusion

This work presents a novel PDMS–$CaCO_3$ microfluidic chip that successfully mimics carbonate surface chemistry, enabling direct visualization of pore-scale displacement while maintaining mechanical and optical performance. The proposed seawater–concrete–CO_2 solution demonstrated promising enhanced oil recovery performance when compared to SDS flooding, despite lacking any synthetic surfactants. Contact angle measurements confirmed the oil-wet nature of the fabricated surface, with an average static contact angle of 138.6° in DI water and 130.9° in seawater, validating its similarity to carbonate reservoir wettability. In the homogeneous porous network, four fluids were tested: DI water, seawater, seawater–concrete–CO_2, and SDS, which achieved oil recoveries of approximately 10%, 15%, 21%, and 25%, respectively. In the randomly structured network, SDS flooding achieved a 39.98% recovery rate, while the seawater–concrete–CO_2 solution yielded a 30.40% recovery rate, confirming its effectiveness under complex flow conditions. Time-resolved visual analysis further revealed distinct mechanisms: SDS facilitated continuous interface advancement, while the seawater–concrete–CO_2 and DI water solutions demonstrated localized surface cleaning, likely driven by ion-mediated adsorption. Overall, the PDMS–$CaCO_3$ micromodel offers a robust and versatile platform for investigating the coupled roles of surface chemistry, fluid formulation, and pore structure in sustainable oil recovery applications.

Although these experiments were conducted at room pressure and temperature, and with larger pore sizes than recent rock-on-chip studies, this setup was intentionally

chosen to isolate the chemical effects and directly observe displacement before transitioning to more realistic confined conditions.[43] However, this study cannot analyze the thermally driven and confinement-dependent mechanisms relevant to *in situ* reservoirs. Therefore, future work can focus on studies at elevated pressure and temperature with smaller rock pore structures to achieve conditions closer to those found in realistic reservoirs.

Conflicts of interest

The authors declare no conflicts of interest.

Data availability

The data supporting this article have been included as part of the supplementary information (SI). The SI video shows the transient change of the contact angle of oil on the PDMS–$CaCO_3$ surface. Other data supporting this study, including raw contact angle measurements, fluorescence microscopy images, MATLAB image analysis scripts, and oil recovery data, are not publicly available but can be obtained upon reasonable request.

Supplementary information is available. See DOI: https://doi.org/10.1039/d5lc00775e.

Acknowledgements

A. R. and M. K. acknowledge financial support from the U.S. National Science Foundation (award #: 2207642), FAU I-SENSE/Engineering Seed grant, and FAU Office of Undergraduate Research & Inquiry.

References

1 International Energy Agency, *Global Energy Review 2025*, IEA, Paris, 2025, p. 5, Available from: https://www.iea.org/reports/global-energy-review-2025.
2 V. B. Malozyomov, N. V. Martyushev, V. V. Kukartsev, V. S. Tynchenko, V. V. Bukhtoyarov, X. Wu, Y. A. Tyncheko and V. A. Kukartsev, Overview of methods for enhanced oil recovery from conventional and unconventional reservoirs, *Energies*, 2023, **16**(13), 4907.
3 M. F. Hamza, C. M. Sinnathambi and Z. M. A. Merican. Recent advancement of hybrid materials used in chemical enhanced oil recovery (CEOR): A review, in *IOP Conference Series: Materials Science and Engineering*, IOP Publishing, 2017, vol. 206, no. 1, p. 012007.
4 F. Bordeaux Rego, V. E. Botechia and D. J. Schiozer, Heavy oil recovery by polymer flooding and hot water injection using numerical simulation, *J. Pet. Sci. Eng.*, 2017, **153**, 187–196.
5 S. Gogoi and S. B. Gogoi, Review on microfluidic studies for EOR application, *J. Pet. Explor. Prod. Technol.*, 2019, **9**(3), 2263–2277.
6 N. S. K. Gunda, B. Bera, N. K. Karadimitriou, S. K. Mitra and S. Majid Hassanizadeh, Reservoir-on-a-Chip (ROC): A new paradigm in reservoir engineering, *Lab Chip*, 2011, **11**(22), 3785–3792.
7 K. Fan, C. Guo, N. Liu, X. Liang, B. Lin and T. Liu, Review and perspectives of microfluidic chips in energy geology, *Phys. Fluids*, 2025, **37**(7), 071301.
8 C. D. Tsakiroglou and D. G. Avraam, Fabrication of a new class of porous media models for visualization studies of multiphase flow processes, *J. Mater. Sci.*, 2002, **37**(2), 353–363.
9 W. Yun, C. M. Ross, S. Roman and A. R. Kovscek, Creation of a dual-porosity and dual-depth micromodel for the study of multiphase flow in complex porous media, *Lab Chip*, 2017, **17**(8), 1462–1474.
10 A. Alomier, D. Cha, S. Ayirala, A. Al-Yousef and H. Hoteit, Novel fabrication of mixed wettability micromodels for pore-scale studies of fluid–rock interactions, *Lab Chip*, 2024, **24**(4), 882–895.
11 P. A. Godoy, A. Orujov, A. P. Gramatges and S. A. Aryana, Rock-on-a-chip: a novel method for designing representative microfluidic platforms based on real rock structures and pore network modelling, *Lab Chip*, 2025, **25**(13), 3109–3122.
12 A. Ratanpara and M. Kim, Wettability Alteration Mechanisms in Enhanced Oil Recovery with Surfactants and Nanofluids: A Review with Microfluidic Applications, *Energies*, 2023, **16**(24), 1–42.
13 S. G. Lee, H. Lee, A. Gupta, S. Chang and P. S. Doyle, Site-selective in situ grown calcium carbonate micromodels with tunable geometry, porosity, and wettability, *Adv. Funct. Mater.*, 2016, **26**(27), 4896–4905.
14 I. K. Shaik, L. Zhang, S. Pradhan, A. K. Kalkan, C. P. Aichele and P. K. Bikkina, A parametric study of layer-by-layer deposition of CaCO3 on glass surfaces towards fabricating carbonate reservoirs on microfluidic chips, *J. Pet. Sci. Eng.*, 2021, **198**, 108231.
15 R. Musabbir Rahman, E. Niemur, G. Blois, F. Kazemifar, M. Kim and Y. Li, A novel microfluidic approach to quantify pore-scale mineral dissolution in porous media, *Sci. Rep.*, 2025, **15**(1), 6342.
16 A. K. Singh, Polydimethylsiloxane based sustainable hydrophobic/oleophilic coatings for oil/water separation: a review, *Cleaner Mater.*, 2022, **6**, 100136.
17 J. N. Lee, C. Park and G. M. Whitesides, Solvent compatibility of poly (dimethylsiloxane)-based microfluidic devices, *Anal. Chem.*, 2003, **75**(23), 6544–6554.
18 Q. Xie, A. Sari, W. Pu, Y. Chen, P. V. Brady, N. Al Maskari and A. Saeedi, pH effect on wettability of oil/brine/carbonate system: Implications for low salinity water flooding, *J. Pet. Sci. Eng.*, 2018, **168**, 419–425.
19 P. Zhang, M. T. Tweheyo and T. Austad, Wettability alteration and improved oil recovery by spontaneous imbibition of seawater into chalk: Impact of the potential determining ions Ca2+, Mg2+, and SO42−, *Colloids Surf., A*, 2007, **301**(1–3), 199–208.
20 J. Zhu, Uncertainty of Kozeny–Carman Permeability Model for Fractal Heterogeneous Porous Media, *Hydrology*, 2023, **10**(1), 21, DOI: 10.3390/hydrology10010021.

21 M. Matyka, A. Khalili and Z. Koza, Tortuosity-porosity relation in porous media flow, *Phys. Rev. E:Stat., Nonlinear, Soft Matter Phys.*, 2008, **78**(2 Pt 2), 026306, DOI: 10.1103/PhysRevE.78.026306, Epub 2008 Aug 25, PMID: 18850935.
22 S. Zhang, H. Yan, J. Teng and D. Sheng, A mathematical model of tortuosity in soil considering particle arrangement, *Vadose Zone J.*, 2020, **19**(1), e20004.
23 T. Ozgumus, M. Mobedi and U. Ozkol, Determination of Kozeny constant based on porosity and pore to throat size ratio in porous medium with rectangular rods, *Eng. Appl. Comput. Fluid Mech.*, 2014, **8**(2), 308–318.
24 S. Nie, P. Liu, K. Chen, W. Wang, Y. Chen and B. Bate, Permeability of structured porous media: numerical simulations and microfluidic models, *J. Zhejiang Univ., Sci., A*, 2024, **25**(12), 1018–1036.
25 J. C. McDonald, D. C. Duffy, J. R. Anderson, D. T. Chiu, W. Hongkai, O. J. A. Schueller and G. M. Whitesides, Fabrication of microfluidic systems in poly (dimethylsiloxane), *Electrophoresis*, 2000, **21**(1), 27–40.
26 A. Ratanpara, J. G. Ricca, A. Gowda, A. Abraham, S. Wiskoff, V. Zauder, R. Sharma, M. Hafez and M. Kim, Towards green carbon capture and storage using waste concrete-based seawater: A microfluidic analysis, *J. Environ. Manage.*, 2023, **345**, 118760.
27 A. Ivanova, A. Orekhov, S. Markovic, S. Iglauer, P. Grishin and A. Cheremisin, Live imaging of micro and macro wettability variations of carbonate oil reservoirs for enhanced oil recovery and CO2 trapping/storage, *Sci. Rep.*, 2022, **12**(1), 1262.
28 M. Behrang, S. Hosseini and N. Akhlaghi, Effect of pH on interfacial tension reduction of oil (Heavy acidic crude oil, resinous and asphaltenic synthetic oil)/low salinity solution prepared by chloride-based salts, *J. Pet. Sci. Eng.*, 2021, **205**, 108840.
29 K. R. Bajgiran, H. C. Hymel, S. Sombolestani, N. Dante, N. Safa, J. A. Dorman, D. Rao and A. T. Melvin, Fluorescent visualization of oil displacement in a microfluidic device for enhanced oil recovery applications, *Analyst*, 2021, **146**(22), 6746–6752.
30 O. Vizika, D. G. Avraam and A. C. Payatakes, On the role of the viscosity ratio during low-capillary-number forced imbibition in porous media, *J. Colloid Interface Sci.*, 1994, **165**(2), 386–401.
31 R. Lenormand, E. Touboul and C. Zarcone, Numerical models and experiments on immiscible displacements in porous media, *J. Fluid Mech.*, 1988, **189**, 165–187.
32 S. Asadabadi, M. Kharazi and J. Saien, Salinity and alkalinity impacts on the interfacial activity of crude oil–water systems using individual and mixtures of a surface-active ionic liquid and conventional surfactant, *RSC Adv.*, 2025, **15**(43), 36050–36064.
33 K. Zhang, A. Georgiadis and J. M. Trusler, Measurements and interpretation of crude Oil-Water/Brine dynamic interfacial tension at subsurface representative conditions, *Fuel*, 2022, **315**, 123266.
34 C. Li, J. Miller, J. Wang, S. S. Koley and J. Katz, Size distribution and dispersion of droplets generated by impingement of breaking waves on oil slicks, *J. Geophys. Res.:Oceans*, 2017, **122**(10), 7938–7957.
35 P. J. Brandvik, P. S. Daling, F. Leirvik and D. F. Krause, Interfacial tension between oil and seawater as a function of dispersant dosage, *Mar. Pollut. Bull.*, 2019, **143**, 109–114.
36 A. Abdi, M. Awarke, M. R. Malayeri and M. Riazi, Interfacial tension of smart water and various crude oils, *Fuel*, 2024, **356**, 129563.
37 R. Lenormand, Liquids in porous media, *J. Phys.: Condens. Matter*, 1990, **2**(S), SA79.
38 N. B. Lu, C. A. Browne, D. B. Amchin, J. K. Nunes and S. S. Datta, Controlling capillary fingering using pore size gradients in disordered media, *Phys. Rev. Fluids*, 2019, **4**(8), 084303.
39 T. Pak, I. Butler, S. Geiger, M. van Dijke and K. Sorbie, Droplet fragmentation: 3D imaging of a previously unidentified pore-scale process during multiphase flow in porous media, *Proc. Natl. Acad. Sci. U. S. A.*, 2015, **112**(7), 1947–1952.
40 R. Gharibshahi, A. Jafari, A. Haghtalab and M. S. Karambeigi, Application of CFD to evaluate the pore morphology effect on nanofluid flooding for enhanced oil recovery, *RSC Adv.*, 2015, **5**(37), 28938–28949.
41 X. Zhao, Y. Feng, G. Liao and W. Liu, Visualizing in-situ emulsification in porous media during surfactant flooding: A microfluidic study, *J. Colloid Interface Sci.*, 2020, **578**, 629–640.
42 A. Rezaei, H. Abdollahi, Z. Derikvand, A. Hemmati-Sarapardeh, A. Mosavi and N. Nabipour, Insights into the effects of pore size distribution on the flowing behavior of carbonate rocks: Linking a nano-based enhanced oil recovery method to rock typing, *Nanomaterials*, 2020, **10**(5), 972.
43 F. Dawaymeh, E. Ayoub, M. Khaleel and N. Alamoodi, Insights into the Application of Microfluidic Platforms in Enhanced Oil Recovery, *Petroleum*, 2025, **11**(4), 422–439.

